ChemComm

COMMUNICATION

View Article Online
View Journal | View Issue

Cite this: *Chem. Commun.*, 2026, **62**, 9932

Received 30th March 2026,
Accepted 21st April 2026

DOI: 10.1039/d6cc01926a

rsc.li/chemcomm

Ni_4N interspersed Ru for enhanced hydrogen oxidation reaction in alkaline media

Anagha Usha Vijayakumar,† Manoj Shanmugasundaram,† Vineesh Thazhe Veettil and David Zitoun *

We report a Ru–Ni_4N/C heterostructured catalyst, prepared by selective Ni nitridation during RuNi alloy annealing in NH_3. It outperforms Pt/C, RuNi alloy and Ru/C in the alkaline hydrogen oxidation reaction (HOR), with a specific activity of 0.4 mA cm^{-2} at 0.1 V *vs.* RHE, twice that of Ru/C, due to optimized H binding energy and enhanced water adsorption *via* Ni alloying and heterostructure formation.

Proton exchange membrane fuel cells (PEMFCs) and anion exchange membrane fuel cells (AEMFCs), operating in acidic and alkaline media, respectively, are the focal points of green energy production. The two vital reactions underpinning these fuel cells are the oxygen reduction reaction (ORR) and the hydrogen oxidation reaction (HOR).[1,2] A hindrance to the commercialization of fuel cells is the high loading of precious metal-based catalysts (Pt based materials).[3] While in PEMFCs an ultra-low loading of Pt enables remarkable HOR performance, high Pt loadings are required to compensate for the sluggish ORR kinetics. AEMFCs outperform PEMFCs by operating in less corrosive environments and enabling the use of non-Pt based catalysts for the ORR. The ORR activity of non-precious metal catalysts is on par with the platinum group metals (PGMs).[4] However, there emerges a new challenge: the HOR kinetics on Pt surfaces are two orders of magnitude lower than in acidic media, necessitating a higher loading.[5] These sluggish kinetics necessitate considerable research dedicated to the development of alternative HOR catalysts for alkaline fuel cells.

Alkaline media allow the use of non-precious metals as electrocatalysts. However, tailoring non-precious metal centres, which satisfies the energy demands, is still a big challenge on the anode side. H_2 adsorbs and dissociates as hydrides on most transition metal surfaces with heats of chemisorption between 60 and 120 kJ mol^{-1}.[6] Among all these transition metals, Ni-based materials, as non-precious metal centres, can activate the slow reactions of hydrogen, *i.e.*, HER and HOR.[7–9] Nickel nitrides and carbides have been reported as good HER and HOR electrocatalysts at low potential; however, their HOR activity is limited by their stability upon anodic polarization (potential breakdown).[10–13] Indeed, the surface oxidation of nickel-based phase (including nitrides and carbides) in alkaline media inhibits the HOR activity. Therefore, the durability of these earth-abundant HOR catalysts is thermodynamically questionable.

On the other hand, recent studies on HOR catalysts suggest that an improvement in activity and stability can be achieved by the addition of foreign metal atoms either segregated on the surface of PGMs or in the form of bimetallic alloys.[5,14–17] Consequently, alloying or partial coating of low-cost transition metals with a small amount of PGMs is a promising way for developing high-activity, low-cost and durable HOR electrocatalysts for AEMFCs.[5,18–22] With the exception of Pt, the electrocatalytic activity of Ru is one of the highest among the pure metals for the HOR. Ru is oxophilic and has a moderate hydrogen adsorption free energy. The electrocatalytic activity of pure Ru is still lower than that of Pt, which prevents it from being used directly in fuel cells. In recent years, great efforts have been dedicated to improving the activity of Ru by surface modification and alloying.[23–26] Alloying of Ru with other transition metals (Ni, Co, Fe and Mn) has been recognized as an effective strategy to enhance the electrocatalytic activity and to reduce the cost.[14] Bimetallic Ru systems have been extensively explored for the HOR in the past few years. Among them, alloying Ru with Ni has great potential to improve the kinetics of HOR/HER.[27–32] DFT studies on the alloying effect of nickel have demonstrated that it reduces the hydrogen binding energy and energy barrier of water formation.[5,33] The oxophilicity of Ni benefits the HOR activity of Ru. In addition to alloying, surface structure modifications such as heterostructuring and interface engineering have shown success in fine-tuning the hydrogen binding energy and water adsorption. Yanrong *et al.*[28]

Department of Chemistry, Bar-Ilan Institute of Nanotechnology and Advanced Materials (BINA), Israel National Institute for Energy Storage (INIES), Bar-Ilan University, Ramat Gan, 5290002, Israel. E-mail: david.zitoun@biu.ac.il
† Equal contribution.

demonstrated that RuNi alloy after annealing in air exhibits improved catalytic performance owing to the formation of surface oxides. The surface nickel oxides play an active role in enhancing water adsorption, while the metallic nickel mitigates the excessively strong hydrogen binding energy. Interface chemistry and heterostructuring were effectively manipulated to deliver a better HOR performance for Pt/NiO by virtue of a decreased HBE after annealing. In contrast to oxides which are either semiconducting or insulating, metal nitrides which are intrinsically metallic are more promising. In this context, interface engineering of metals with Ni_3N enabled a close to ideal ΔG_{H^*} value.[11,31,34]

In this study, we synthesized Ru–Ni alloys on Vulcan carbon by a wet impregnation followed by thermal reduction method. Further annealing under ammonia yielded Ru–Ni_4N/C dealloyed heterostructures. Ru–Ni_4N/C heterostructures showed better performance toward the HOR in comparison to their alloy counterparts and even compared to Pt/C. This study opens a new platform for the synthesis of highly active HOR catalysts by interface engineering.

Fig. 1(A) displays TEM images of the synthesized catalysts (1. RuNi-7030, 2. RuNi-8515, 3. $RuNi_4N$-7030 and 4. $RuNi_4N$-8515), revealing uniformly dispersed nanoparticles on the carbon support with an average size of ~2.2 nm. Remarkably, the particle size further decreases after annealing at 350 °C in NH_3, which can be attributed to mild surface etching by ammonia and the formation of thermodynamically stable nickel nitride phases that induce lattice contraction and structural rearrangement. Fig. 1B shows the high-angle annular dark field scanning transmission electron microscopy (HAADF-STEM) image, elemental maps and line-scan profile of a representative $RuNi_4N$-8515 nanoparticle, evidencing a homogeneous distribution of Ru and Ni across the particle. The overlapped elemental maps confirm homogeneous mixing of two metals, while similarly mapping for $RuNi_4N$-7030/C (Fig. S1) demonstrates similarly uniform Ru and Ni dispersion. Together with the presence of N signals in both the nanoparticles and carbon regions, these data indicate that NH_3 treatment leads to nitrogen incorporation into the metal phase as well as N-doping of the carbon support. The energy dispersive X-ray spectroscopy (EDX) line profile in Fig. 1B confirms the coexistence of Ru and Ni within individual nanoparticles. Bulk elemental compositions derived from high resolution scanning electron microscopy (HRSEM)–EDX (Table S1) agree well with the nominal feed ratios, further supporting the successful synthesis of composition-tuned RuNi and RuNiN catalysts. Additional TEM images of all catalysts (Fig. S2) consistently show a uniform nanoparticle distribution over the carbon matrix, providing a high density of accessible active sites for the HOR. The ammonia treatment preserves the high dispersion and small particle size of the samples (Fig. S3).

The crystal structure of the catalysts was examined by powder X-ray diffraction (XRD, Fig. 2). In contrast to Ru/C, RuNi-7030/C and RuNi-8515/C samples do not show distinct diffraction peaks, which is likely due to their relatively low metal loadings and the ultrasmall particle size.

After NH_3 treatment at 350 °C, Ni reacts with nitrogen to form Ni_4N, and diffraction peaks characteristic of the RuNi alloy and the Ni_4N phase emerge for RuNi-7030/C (denoted as $RuNi_4N$-7030/C, Fig. 2b). By comparison, no clear diffraction peaks are observed for NH_3-treated RuNi-8515/C ($RuNi_4N$-8515/C), consistent with its lower Ni content. Furthermore, no additional reflections assignable to Ru nitrides are detected, indicating that N incorporation into the Ru lattice (RuN formation) does not occur under these conditions.

X-ray photoelectron spectroscopy (XPS) was employed to probe the surface composition and chemical states of $RuNi_{4n}$/C catalysts, including RuNi-7030/C, RuNi-8515/C, and their nitride analogues. High-resolution XPS spectra of $RuNi_4N$-8515 and $RuNi_4N$-7030 are displayed in Fig. 3A and B, respectively. In the Ru 3p spectrum of Ru/C, a peak at 462.3 eV corresponds to metallic Ru $3p_{3/2}$ (Fig. S4) but it appears at a higher binding energy than bulk Ru (461.4 eV), reflecting strong metal–support interactions with carbon. The higher electronegativity of carbon (2.55) relative to Ru (2.2) withdraws electron density from Ru, leading to an upshift in biding energy. Additional peaks at 466.0 eV and 470.8 eV are assigned to surface-oxidized Ru^{4+} species and the satellite peak, respectively.

For RuNi-7030/C and RuNi-8515/C, the Ni 2p spectra exhibit metallic Ni $2p_{3/2}$ peaks at 853.8 and 853.7 eV, respectively

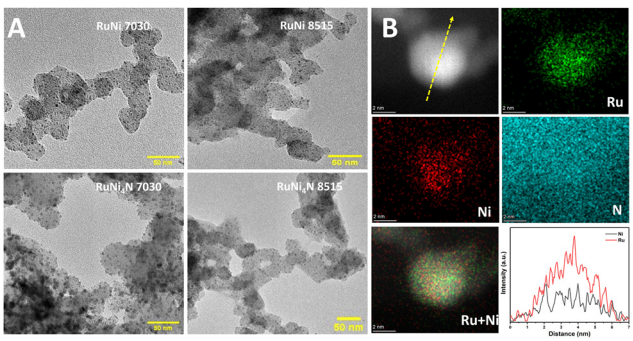

Fig. 1 Electron microscopy images. (A) Transmission electron microscopy (TEM) images of (1) RuNi-7030, (2) RuNi-8515, (3) $RuNi_4N$-7030 and (4) $RuNi_4N$-8515. (B) High angle annular dark field-scanning transmission electron microscopy elemental mapping of $RuNi_4N$-8515 and line profile mapping of Ru and Ni (yellow dotted line) nanoparticles.

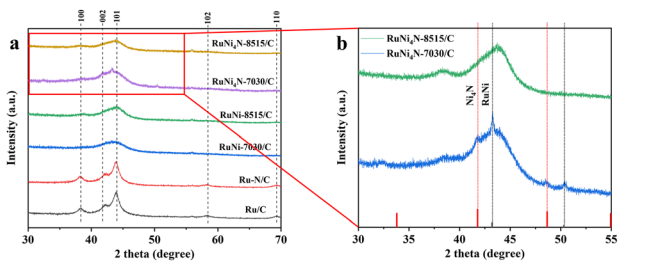

Fig. 2 (a) XRD patterns of Ru/C, Ru-N/C, RuNi-7030/C, RuNi-8515/C, $RuNi_4N$-7030/C and $RuNi_4N$-8515/C. (b) Enlarged XRD patterns of $RuNi_4N$-7030 and $RuNi_4N$-8515, highlighting RuNi- and Ni_4N-related diffraction features.

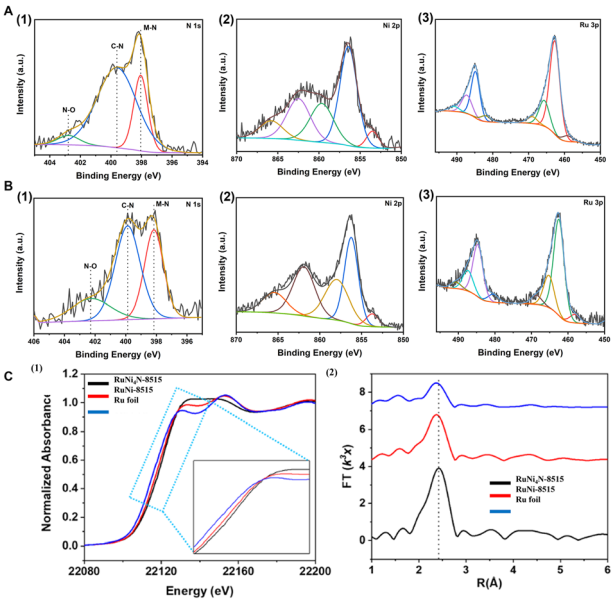

Fig. 3 Surface and local structural characterization. (A) High-resolution XPS spectra of $RuNi_4N$-8515/C: (1) N 1s, (2) Ni 2p, and (3) Ru 3p. (B) High-resolution XPS spectra of $RuNi_4N$-7030/C: (1) N 1s, (2) Ni 2p, and (3) Ru 3p. (C) Ru K-edge XAS: (1) normalized XANES spectra and (2) magnitude of Fourier-transformed EXAFS for RuNi-8515/C, $RuNi_4N$-8515/C, and Ru foil.

(Fig. S5 and S6), while the corresponding Ru 3p metallic peaks are further shifted to 462.4 and 462.5 eV, evidencing electronic perturbation of Ru induced by Ni incorporation.[27,30,31] The N 1s spectra (Fig. 3A1 and B1) confirm nitrogen incorporation into both the metal and the carbon matrix, as indicated by M–N and C–N contributions. In the nitride samples $RuNi_4N$-7030 and $RuNi_4N$-8515 (Fig. 3A2 and B2), Ni 2p peaks shift to lower binding energy relative to their non-nitride counterparts, whereas Ru 3p peaks at 462.6 eV and 462.8 eV (Fig. 3A3 and B3) shift to higher binding energy. These opposite shifts point to substantial reorganization of the Ru–Ni electronic structure upon N-doping.

To further elucidate the electronic and geometric structure of Ru, Ru K-edge X-ray absorption spectroscopy (XAS) was carried out for RuNi-8515, $RuNi_4N$-8515, and Ru foil. The normalized X-ray absorption near-edge structure (XANES) spectra (Fig. 3C1) display an increased white-line intensity and a positive absorption edge shift for the RuNi alloy compared with Ru foil. Fourier-transform (FT) extended X-ray absorption fine structure (EXAFS) spectra in *R*-space (Fig. 3C2) show a main peak at 2.42 Å for Ru foil, whereas RuNi-8515/C and $RuNi_4N$-8515/C exhibit a peak at ~2.36 Å assignable to Ru–Ni coordination.[29,31] The Ru K-edge FT-EXAFS spectrum of $RuNi_4N$-8515/C corresponds to a statistical alloy. Upon quantitative fitting, this feature is assigned to Ru–Ni with a coordination number (CN) of 6, an amplitude reduction factor (S_0^2) of 0.938, a Debye–Waller factor (σ^2) of 0.00402 Å^2, and a phase-corrected bond distance (R) of 2.67 Å. The small difference of 0.3 Å between the FT peak position and the fitted distance arises from the EXAFS phase shift, within the typical range reported for transition-metal K-edge EXAFS (Fig. S9). The relatively small σ^2 value reflects a swell-ordered first coordination shell, suggesting a uniform local Ru–Ni environment.

Cyclic voltammetry was conducted in N_2-saturated 0.1 M KOH to probe the electrochemical surface features of the $RuNi_4N$/C catalysts. As shown in Fig. 4a, Pt/C displays the characteristic hydrogen underpotential deposition (H-UPD) region of Pt, with distinct peaks associated with different planes, together with a well-defined double layer and surface redox features. The first H-UPD peak of Pt/C appears at 0.28 V *vs.* RHE, whereas Ru/C shows a pronounced H-UPD peak at 0.14 V *vs.* RHE, and the peaks of RuNi-8515/C and $RuNi_4N$-8515/C shift further to 0.13 V and 0.12 V *vs.* RHE, respectively, indicating alloying and nitridation-induced modification of the hydrogen adsorption properties and active surface sites. Linear sweep voltammetry (LSV) in H_2-saturated 0.1 M KOH reveals the steady-state HOR performance (Fig. 4b). All Ru-based catalysts outperform Pt/C up to ~0.15 V *vs.* RHE, delivering higher geometric current densities (j_{geo}) that highlight the intrinsic suitability of Ru surfaces for alkaline HOR (Fig. S7). Among them, $RuNi_4N$-8515/C exhibits the most positive onset potential and the highest j_{geo} across the low overpotential region, surpassing $RuNi_4N$-7030/C, RuNi-8515/C, RuNi-7030/C, and Ru/C, consistent with its optimized composition and surface chemistry.

To quantitatively benchmark intrinsic HOR performance, specific activities (ECSA-normalized) and mass activities were evaluated at 100 mV. From copper underpotential deposition (Cu UPD) stripping voltammetry (Fig. S8), an ECSA value of 108.2 m^2 g^{-1} is obtained for $RuNi_4N$-8515 and a highest value of 250 m^2 g^{-1} is observed for $RuNi_4N$-7030 (Table S2). $RuNi_4N$-8515 exhibits the highest specific activity of 0.4 mA cm^{-2} and a mass activity of 156 A g_{Ru}^{-1}, surpassing all counterparts: Ru/C (0.2 mA cm^{-2}, 112 A g^{-1}), RuNi-7030 (0.003 mA cm^{-2}, 125 A g^{-1}), RuNi-8515 (0.3 mA cm^{-2}, 131 A g^{-1}), and $RuNi_4N$-7030 (0.18 mA cm^{-2}, 147 A g^{-1}). Despite $RuNi_4N$-7030's superior ECSA (250 m^2 g^{-1} *vs.* 108 m^2 g^{-1} for $RuNi_4N$-8515), its lower specific activity reveals that surface abundance alone cannot account for the performance hierarchy, and that the optimal Ru : Ni ratio (85 : 15) combined with N-doping in $RuNi_4N$-8515 maximizes intrinsic activity per Ru site over Ru/C.

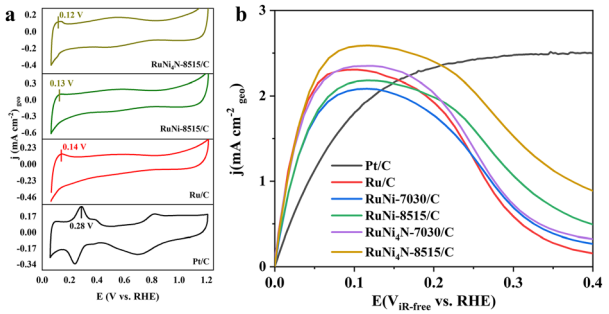

Fig. 4 Electrochemical performance. (a) CV curves of Pt/C, Ru/C, RuNi-8515/C and $RuNi_4N$-8515/C. (b) LSV polarization curves of Pt/C, Ru/C RuNi-7030/C, RuNi-8515/C, $RuNi_4N$-7030/C and $RuNi_4N$-8515/C at 10 mV s^{-1}.

This trend is consistent with the XPS/XAS evidence for electronic structural tuning of Ru–Ni centers. The progressive positive shift of the Ru 3p binding energy from Ru/C (462.3 eV) to $RuNi_4N$-8515 (462.8 eV) indicates electron withdrawal from Ru by both Ni (*via* electronegativity differences) and N-coordination, which weakens overly strong H* binding and brings the hydrogen binding energy closer to the optimum for the HOR. EXAFS analysis confirms Ru–Ni coordination at ~2.36 Å, shorter than Ru–Ru in Ru foil, implying a contracted Ru environment, while the negative shift of Ni 2p after nitridation suggests increased electron density at Ni sites, favoring OH* adsorption that accelerates the Volmer step in alkaline HOR. The combined effects of tuned HBE on Ru, optimized OH binding at Ni/N sites, and a high density of accessible Ru–Ni ensembles lead to Pt-competitive HOR kinetics for $RuNi_4N$-8515/C and establish a clear structure–activity relationship for PGM-free alkaline HOR catalysts.

A previous DFT study on Ru-based HER catalysts[35] has shown that Ru is on the strong-H-binding side of the ΔG_{H^*} volcano. Alloying with Ni[35] and support interactions with nitride downshift the Ru d-band centre and bring ΔG_{H^*} closer to the optimum. For alkaline HOR, optimized H* adsorption is also required to balance rapid H_2 dissociation with facile H* desorption, while suitable OH* binding at neighbouring oxophilic sites is needed to accelerate the Volmer step. In the $RuNi_4N$-8515/C catalyst, the positive shift of Ru 3p binding energy, the contracted Ru–Ni coordination from EXAFS and the H-UPD shift to lower potential correlate with the DFT-derived trend. These experimental signatures therefore provide indirect but compelling support for the conclusion that the enhanced HOR activity of $RuNi_4N$-8515/C arises from optimized adsorption/desorption behaviour at Ru–Ni–N interfacial sites, beyond the alloying effect reported previously.[36]

In conclusion, Pt-free RuNi alloy and $RuNi_4N$/C catalysts deliver superior alkaline HOR performance through precise electronic and structural tuning. Nitriding optimizes Ru hydrogen binding energy while enhancing Ni mediated water dissociation, yielding marked gains in specific activity (0.4 mA cm^{-2}) and mass activity (156 A g^{-1}) at 0.1 V *vs.* RHE for $RuNi_4N$-8515. While the 85 : 15 Ru : Ni ratio maximizes intrinsic activity per site, 70 : 30 compositions offer enhanced stability, revealing a composition–performance trade-off. XAFS confirms that these effects arise from Ru–Ni coordination (2.36 Å) and the N-modified electronic structure, establishing a clear structure–activity relationship for PGM-free HOR anodes.

Conflicts of interest

There are no conflicts to declare.

Data availability

All data presented in this article are available in the manuscript.

Supplementary information (SI) is available. See DOI: https://doi.org/10.1039/d6cc01926a.

References

1 P. P. Edwards, V. L. Kuznetsov, W. I. F. David and N. P. Brandon, *Energy Policy*, 2008, **36**, 4356–4362.
2 L. Zhang, C. Jia, F. Bai, W. Wang, S. An, K. Zhao, Z. Li, J. Li and H. Sun, *Fuel*, 2024, 129455.
3 O. Lori and L. Elbaz, *ChemCatChem*, 2020, **12**, 3434–3446.
4 G. A. Goenaga, A. L. Roy, N. M. Cantillo, S. Foister and T. A. Zawodzinski, *J. Power Sources*, 2018, **395**, 148–157.
5 L. Zhao, H. Liu, Y. Liu, X. Han, J. Xu, W. Xing and W. Guo, *ACS Appl. Mater. Interfaces*, 2020, **12**, 40248–40260.
6 C. A. Campos-Roldán and N. Alonso-Vante, *Electrochem. Energy Rev.*, 2019, **2**, 312–331.
7 A. G. Oshchepkov, G. Braesch, A. Bonnefont, E. R. Savinova and M. Chatenet, *ACS Catal.*, 2020, **10**, 7043–7068.
8 Z. Zhou, Y. Liu, J. Zhang, H. Pang and G. Zhu, *Electrochem. Commun.*, 2020, **121**, 106871.
9 S. Bulakhe, N. Shinde, J. S. Kim, R. S. Mane and R. Deokate, *Int. J. Energy Res.*, 2022, **46**, 17829–17847.
10 T. Wang, M. Wang, H. Yang, M. Xu, C. Zuo, K. Feng, M. Xie, J. Deng, J. Zhong, W. Zhou, T. Cheng and Y. Li, *Energy Environ. Sci.*, 2019, **12**, 3522–3529.
11 L. Su, D. Gong, N. Yao, Y. Li, Z. Li and W. Luo, *Adv. Funct. Mater.*, 2021, **31**, 1–8.
12 W. Ji, C. Zhan, D. Li, Y. Xu, Y. Zhang, L. Wang, L. Liu, Y. Wang, W. Chen, H. Geng and X. Huang, *J. Mater. Chem. A*, 2021, **9**, 26323–26329.
13 A. Munir, T. ul Haq, M. Saleem, A. Qurashi, S. Z. Hussain, F. Sher, A. Ul-Hamid, A. Jilani and I. Hussain, *Electrochim. Acta*, 2020, **341**, 136032.
14 H. Wang, Y. Yang, F. J. Disalvo and H. D. Abrunã, *ACS Catal.*, 2020, **10**, 4608–4616.
15 M. Alesker, I. Bakos, V. Davies, Q. Jia, L. Burlaka, V. Yarmiayev, A. Muzikansky, A. Kitayev, M. Page, S. Mukerjee and D. Zitoun, *Catal. Sci. Technol.*, 2021, **11**, 1337–1344.
16 M. Shviro, S. Polani, R. E. Dunin-Borkowski and D. Zitoun, *Adv. Mater. Interfaces*, 2018, **5**, 1701666.
17 V. T. Veettil, M. Shanmugasundaram and D. Zitoun, *Energy Adv.*, 2024, **3**, 2896–2902.
18 V. R. Stamenkovic, B. S. Mun, K. J. J. Mayrhofer, P. N. Ross and N. M. Markovic, *J. Am. Chem. Soc.*, 2006, **128**, 8813–8819.
19 C. Silva-Carrillo, E. A. Reynoso-Soto, J. R. Flores-Hernández, B. Trujillo-Navarrete, M. I. Salazar-Gastelum, T. R. Castañon, S. Perez-Sicairos, J. M. Romo-Herrera and R. M. Félix-Navarro, *Top. Catal.*, 2022, **65**, 1251–1261.
20 L. Wang, S. Meng, C. Tang, C. Zhan, S. Geng, K. Jiang, X. Huang and L. Bu, *ACS Nano*, 2023, **17**, 17779–17789.
21 C. A. Campos-Roldán, L. Calvillo, G. Granozzi and N. Alonso-Vante, *J. Electroanal. Chem.*, 2020, **857**, 113449.
22 L. An, X. Zhao, T. Zhao and D. Wang, *Energy Environ. Sci.*, 2021, **14**, 2620–2638.
23 Y. Zheng, Y. Jiao, Y. Zhu, L. H. Li, Y. Han, Y. Chen, M. Jaroniec and S. Z. Qiao, *J. Am. Chem. Soc.*, 2016, **138**, 16174–16181.
24 S. St. John, R. W. Atkinson, R. R. Unocic, T. A. Zawodzinski and A. B. Papandrew, *J. Phys. Chem. C*, 2015, **119**, 13481–13487.
25 J. Mahmood, F. Li, S. M. Jung, M. S. Okyay, I. Ahmad, S. J. Kim, N. Park, H. Y. Jeong and J. B. Baek, *Nat. Nanotechnol.*, 2017, **12**, 441–446.
26 Y. Li, J. Abbott, Y. Sun, J. Sun, Y. Du, X. Han, G. Wu and P. Xu, *Appl. Catal., B*, 2019, **258**, 117952.
27 X. Zhang, Z. Li, X. Sun, L. Wei, H. Niu, S. Chen, Q. Chen, C. Wang and F. Zheng, *ACS Mater. Lett.*, 2022, **4**, 2097–2105.
28 Y. Xue, L. Shi, X. Liu, J. Fang, X. Wang, B. P. Setzler, W. Zhu, Y. Yan and Z. Zhuang, *Nat. Commun.*, 2020, **11**, 1–8.
29 J. Mao, C. T. He, J. Pei, Y. Liu, J. Li, W. Chen, D. He, D. Wang and Y. Li, *Nano Lett.*, 2020, **20**, 3442–3448.
30 J. Liu, J. Wang, Y. Fo, B. Zhang, C. Molochas, J. Gao, W. Li, X. Cui, X. Zhou, L. Jiang and P. Tsiakaras, *Chem. Eng. J.*, 2023, **454**, 139959.

31 L. Han, P. Ou, W. Liu, X. Wang, H. T. Wang, R. Zhang, C. W. Pao, X. Liu, W. F. Pong, J. Song, Z. Zhuang, M. V. Mirkin, J. Luo and H. L. Xin, *Sci. Adv.*, 2022, **8**, 1–10.
32 L. Cai, W. Liu, Z. Cao, H. Li, Y. Cong, X. Zhu and W. Yang, *J. Membr. Sci.*, 2020, **599**, 117702.
33 E. S. Davydova, J. Zaffran, K. Dhaka, M. C. Toroker and D. R. Dekel, *Catalysts*, 2018, **8**, 1–19.
34 Z. Liang, H. Liu, S. Huang, M. Xing, Z. Li, S. Wang, L. Yang and D. Cao, *J. Mater. Chem. A*, 2022, **11**, 849–857.
35 L. Han, P. Ou, W. Liu, X. Wang, H.-T. Wang, R. Zhang, C.-W. Pao, X. Liu, W.-F. Pong, J. Song, Z. Zhuang, M. V. Mirkin, J. Luo and H. L. Xin, *Sci. Adv.*, 2022, **8**, eabm3779.
36 X. Fu, Z. Chen, S. Zhang, J. Wang, J. Ding and X. Han, *Small*, 2024, **20**, 2307725.